Cephalogram Synthesis and Landmark Detection in Dental Cone-Beam CT Systems

Yixing Huang, Fuxin Fan, Christopher Syben, Philipp Roser, Leonid Mill, Andreas Maier

Abstract—Due to the lack of standardized 3D cephalometric analytic methodology, 2D cephalograms synthesized from 3D cone-beam computed tomography (CBCT) volumes are widely used for cephalometric analysis in dental CBCT systems. However, compared with conventional X-ray film based cephalograms, such synthetic cephalograms lack image contrast and resolution, which impairs cephalometric landmark identification. In addition, the radiation dose during the scan for 3D reconstruction causes potential health risks. In this work, we propose a sigmoid-based intensity transform that uses the nonlinear optical property of X-ray films to increase image contrast of synthetic cephalograms from 3D volumes. To improve image resolution, super resolution deep learning techniques are investigated. For low dose purpose, the pixel-to-pixel generative adversarial network (pix2pixGAN) is proposed for 2D cephalogram synthesis directly from two CBCT projections. For landmark detection in the synthetic cephalograms, an efficient automatic landmark detection method using the combination of LeNet-5 and ResNet50 is proposed. Our experiments demonstrate the efficacy of pix2pixGAN in 2D cephalogram synthesis, achieving an average peak signal-to-noise ratio (PSNR) value of 33.8 with reference to the cephalograms synthesized from 3D CBCT volumes. Pix2pixGAN also achieves the best performance in super resolution, achieving an average PSNR value of 32.5 without the introduction of checkerboard or jagging artifacts. Our proposed automatic landmark detection method achieves 86.7% successful detection rate in the 2 mm clinical acceptable range on the ISBI Test1 data, which is comparable to the state-of-the-art methods. The method trained on conventional cephalograms can be directly applied to landmark detection in the synthetic cephalograms, achieving 93.0% and 80.7% successful detection rate in 4 mm precision range for synthetic cephalograms from 3D volumes and 2D projections respectively.

Index Terms—Cephalogram synthesis, super resolution, landmark detection, deep learning.

I. Introduction

Since the introduction in 1931 by Broadbent [1], cephalometric examination using two-dimensional (2D) lateral cephalograms is a standard procedure for orthodontic diagnostics and treatment planning. In cephalograms, various landmarks are sketched to form lines and angles, which are essential to assess patients' skeletal and dental relationships. Such cephalograms are acquired in specialized radiographic cephalometer systems. Cone-beam computed tomography (CBCT) was introduced to dentistry at the end of last century [2]. Since then it has been playing an very important role in various dental applications [3], including oral surgery,

orthodontics, endodontics, and implant treatment planning. In dentistry, one system capable of multiple functions is a trend to empower dentists, facilitate management and save cost. For this purpose, systems combining CBCT and cephalograms (as well as panoramic radiographs typically) emerged. One approach to achieve such multi-functions is to equip CBCT systems with additional physical modules. However, such systems require additional acquisitions for cephalograms, causing extra dose exposure to patients. Therefore, achieving multi-functions on a standalone CBCT system with one single acquisition, where cephalometric analysis is performed based on CBCT data, is preferable for the sake of low dose and further cost reduction.

CBCT reconstructs a three-dimensional (3D) volume of anatomical structures. For the applications of orthodontics, large field of view (FOV) volumes are typically reconstructed to cover the whole maxillofacial or craniofacial region. In the 3D volume, landmarks can be visualized directly without superimposition and perspective distortion. Therefore, a lot of research work has been conducted to evaluate the measurement accuracy, reliability and reproducibility of 3D landmark identification, in order to justify whether 3D cephalometric analysis is more beneficial than the standard 2D analysis. For example, Park et al. [4] proposed to use 19 landmarks to examine the zygoma, maxilla, mandible and facial convexity and a 3D chart is provided to record measurements. Kamiishi et al. [5] proposed a 3D analysis method using two types of surface rendering. Some systematic reviews on 3D cephalometric analysis are presented in [6]–[8]. However, such 3D cephalometric analysis methods are still under development and mostly limited to research, due to the requirement of special softwares, the lack of standardized analytical methodology and insufficient evidence for diagnostic efficacy [6]. In addition, as practitioners are used to work with conventional 2D cephalograms, it usually takes time for them to gain proficient skills on 3D cephalometric analysis. Therefore, 3D cephalometric analysis is not yet widely used in practice.

Instead, synthesizing 2D cephalograms from 3D CBCT volumes is a widely used practical way for cephalometric analysis in dental CBCT systems [9]–[13]. In such a way, additional physical 2D cephalometer modules are not necessary, while the existing 2D cephalometric databases and standardized methodologies are inherited. Many studies have reported that CBCT synthetic cephalograms are equivalent or even superior to conventional cephalograms in terms of landmark identification error and reproducibility [14]–[16]. However, CBCT synthetic cephalograms typically have different appearance from conventional cephalograms in terms of image contrast

Y. Huang, F. Fan, C. Syben, P. Roser, L. Mill and A. Maier are with Pattern Recognition Lab, Friedrich-Alexander-University Erlangen-Nuremberg, Erlangen, Germany (e-mail: yixing.yh.huang@fau.de).

P. Roser and A. Maier are also with Erlangen Graduate School in Advanced Optical Technologies (SAOT), Erlangen, Germany.
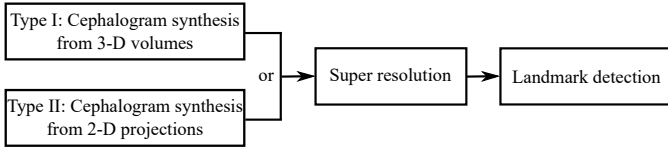
Fig. 1. A brief overview of our contributions to cephalometric analysis in dental CBCT systems.

(see Fig. 2) and resolution, since X-ray films used in conventional cephalograms have nonlinear optical properties [17] and higher image resolution than digital detectors in CBCT systems [18], [19]. Such differences require practitioners to have further training to get familiar with synthetic cephalograms. In addition, although CBCT has lower radiation dose than multi-slice CT, it still requires considerably more projections than conventional 2D cephalograms. Hence, the potential health risks caused by radiation dose is still a concern considering the as-low-as-reasonably-achievable (ALARA) principle.

For cephalometric analysis in synthetic cephalograms, landmark detection is necessary. Manual cephalometric landmark identification is tedious and time-consuming. And intra- and inter-observer variability may lead to unreproducible measurements. Therefore, computer aided automatic landmark detection is highly desired.

In order to address the above mentioned aspects in cephalometric analysis, the following contributions, displayed in Fig. 1 as an overview, are made in this work:

1. Image contrast: a nonlinear sigmoid-based intensity transform according to the optical property of X-ray films is proposed for Type I cephalogram synthesis;
2. Low dose: direct cephalogram synthesis from dual CBCT projections is proposed, where the advantage of using dual projections over one projection, the selection of patches, and the feasibility of one model for multi-quadrant patches are elaborated;
3. Image resolution: super resolution (SR) techniques using different adversarial generative networks (GANs) are investigated;
4. Landmark detection: an efficient automatic landmark detection method is proposed, which is applicable on synthetic cephalograms.

II. RELATED WORK

A. Cephalogram Synthesis

Various methods for cephalogram synthesis from 3D CBCT volumes have been proposed. Ray-sum multi-planar reformatting (MPR), also called ray casting (RayCast), using orthogonal projection was the first reported method [9]–[11]. Since real cephalometer systems use cone-beam X-rays, which cause perspective deformation, Kumar et al. [12] proposed to use perspective projection based on the Wehmer cephalostat geometry into the RayCast method to reproduce conventional cephalometric geometry with similar accuracy. However, they concluded that synthetic cephalograms with orthogonal projection provided greater accuracy of measurement for midsagittal plane dimensions than those with perspective projection. Other

than RayCast methods, maximum intensity projection (MIP) [13] is also used for cephalogram synthesis from 3D CBCT volumes. Since only the largest intensity pixels are projected, low intensity structures are omitted. As a consequence, MIP was proven to produce less reproducible measurements than RayCast.

Synthesizing cephalograms from 2D cone-beam projections is an image-to-image translation problem. Due to the severe perspective deformation in cone-beam projections, it is very challenging to restore such deformation with conventional methods. Recently, deep learning methods, particularly using generative adversarial networks (GANs) [20], have achieved promising results in image synthesis in various medical applications such as 3T MRI images to 7T MRI images [21], PET images to CT images [22], and MRI cone-beam projections to X-ray cone-beam projections [23]. However, to the best of our knowledge, such projection-to-cephalogram synthesis using GANs have not been investigated yet. For parallel-beam projection to cone-beam projection conversion, Syben et al. have proposed a novel rebinning algorithm using known operator learning [24], [25]. It reconstructs an intermediate volume with learnt filters from parallel-beam MRI projections in a specialized trajectory and afterwards reproject the volume with the desired cone-beam geometry to generate CBCT projections. Due to the requirement of the special trajectory and the large number of projections, the method in [24] cannot be applied in our application where direct synthesis of parallel-beam cephalogram from a few number of CBCT projections is desired.

B. Image Super Resolution

Image SR aims at recovering high resolution (HR) images from low resolution (LR) images. Benefiting from the strong capacity of extracting effective high level features between LR and HR images, deep learning has achieved the state-of-the-art performance for various SR applications [26]. One of the first neural networks in this field is called super resolution convolutional neural network (SRCNN) proposed by Dong et al. [27]. It learns the mapping between interpolated low resolution (ILR) images and HR images based on conventional sparse-coding approaches. Follow-up researchers proposed to use deeper neural networks such as the VGG network [28], deep Laplacian pyramid networks [29], and deep residual networks [30], [31]. Although such deep learning methods achieve high peak signal-to-noise ratio (PSNR), generated images still lack high frequency details. That is why adversarial learning is introduced, where a generator network is trained to generate realistic HR images and a discriminator network is trained to tell the difference between generated HR images and target HR images. Super resolution generative adversarial network (SRGAN) [32] is the first introduced GAN-based deep learning method for SR, which became the benchmark method in SR. The generator of SRGAN uses 5 residual blocks. The replacement of these residual blocks by residual dense blocks (RDBs) or residual-in-residual dense blocks (RRDBs) results in two enhanced super resolution generative adversarial networks (ESRGANs) [33], [34]. Both

ESGANs further adjust the architecture design, perceptual loss and adversarial loss of SRGAN to avoid the introduction of different artifacts.

C. Landmark Detection

Many efforts have been devoted to automatic cephalometric landmark detection. In particular, several benchmark methods have been proposed in the challenges organized by the International Symposium on Biomedical Imaging (ISBI) in 2014 [35] and 2015 [36]. The method proposed by Ibragimov et al. [37] applies game theory and random forests, which won the ISBI Challenge 2014 with 72.7% successful detection rate (SDR) within the clinical acceptable 2 mm precision range. The random forest regression-voting method proposed by Lindner and Cootes [38] won the ISBI 2015 challenge with 74.8% 2 mm-SDR. Arik et al. [39] introduced a convolutional neural network (CNN) for landmark detection, achieving 75.3% 2 mm-SDR. In 2019, the CephaNet [40] using the the faster R-CNN architecture as a backbone obtains 82.5% 2 mm-SDR on ISBI Test1 data. Chen et al. [41] proposed a method combining a VGG-19 feature extraction module, an attentive feature pyramid fusion module and a regression-voting module, achieving 86.7% 2 mm-SDR on ISBI Test1 data. The latest method proposed by Song et al. [42] applies the ResNet50 [43] to detect landmarks on region-of-interest (ROI) patches extracted by a registration step, achieving 86.74% 2 mm-SDR on ISBI Test1 data.

III. MATERIALS AND METHODS

In this section, we introduce the contents of Fig. 1 in detail.

A. Type I: Cephalogram Synthesis from 3D CBCT Volumes

For Type I synthesis, our method includes the steps of skeleton enhancement, ray casting, and sigmoid-based transform. For the sigmoid-based transform, the modification from the original sigmoid transform is explained.

1) Skeleton enhancement: We denote the intensity distribution of a patient head by $\boldsymbol{f}(x, y, z)$. We further denote a reconstructed 3D volume of the head by $\tilde{\boldsymbol{f}}(x, y, z)$. In dental CBCT systems, the patient head is typically well aligned by a fixation device. If not, a rigid transform $\vec{T} \in$ SE3 can be applied to $\tilde{\boldsymbol{f}}$ to adjust the orientation of the head facing to the positive Y direction. In cephalograms, the projection of skeletal structures and airways plays an important role. In order to enhance such structures, we choose two thresholds -500 HU and 1000 HU to preprocess $\tilde{\boldsymbol{f}}$ in the following way,

$$\boldsymbol{f}^*(x, y, z) = \begin{cases} a \cdot \tilde{\boldsymbol{f}}(x, y, z), & \text{if } \tilde{\boldsymbol{f}}(x, y, z) > 1000 \text{ HU}, \\ -1000 \text{ HU}, & \text{if } \tilde{\boldsymbol{f}}(x, y, z) < -500 \text{ HU}, \\ \tilde{\boldsymbol{f}}(x, y, z), & \text{otherwise}. \end{cases}$$
(1)

The threshold 1000 HU is used to segment skeletal structures and a is a weight to slightly highlight them. To preserve soft tissue visualization, we empirically choose $a = 1.3$ in this work. By resetting the values below -500 HU to -1000 HU, the noise and artifacts (e.g., scattering and beam hardening artifacts) in the airway areas are suppressed. Any other structures between these two thresholds are mainly soft tissues. Their values are preserved.

(a) Real cephalogram   (b) Synthetic cephalogram
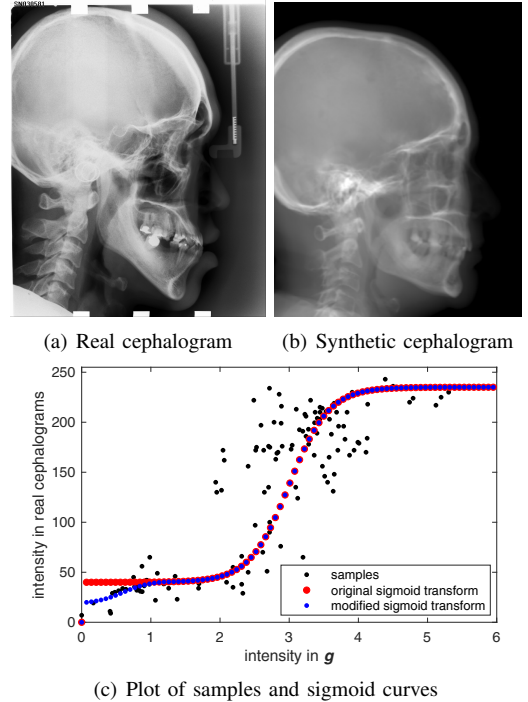
(c) Plot of samples and sigmoid curves

Fig. 2. Image contrast difference between real conventional cephalograms and RayCast synthetic cephalograms: (a) a real cephalogram example; (b) a RayCast synthetic cephalogram example; (c) the plot of samples between RayCast synthetic cephalograms and real cephalograms with a original sigmoid curve (red) and our proposed modified sigmoid curve (blue).

2) Ray casting: According to [9]–[12], RayCast is applied to synthesize preliminary 2D cephalograms from 3D volumes,

$$\boldsymbol{g}(y, z) = \mathcal{P} \boldsymbol{f}^*(x, y, z),$$
(2)

where $\boldsymbol{g}(y, z)$ is an (enhanced) attenuation integral image, and $\mathcal{P}$ is a projection operator. The pixel intensity values of $\boldsymbol{g}$ are typically in the range of approximately [0, 6] for human heads. When using parallel-beam X-rays, $\mathcal{P}$ is an orthogonal projection along the X direction; when using cone-beam X-rays, $\mathcal{P}$ is a perspective projection using the geometry of a standard Wehmer cephalostat [12], i.e., with the isocenter-to-detector distance of 11.5 cm and the source-to-isocenter distance of 152.4 cm. Since synthetic cephalograms with orthogonal projection provide better measurement accuracy than those with perspective projection [12], orthogonal projection is mainly used in this work.

3) Original sigmoid transform: In Fig. 2, one real conventional cephalogram example and one example of $\boldsymbol{g}$ are displayed, where evident image contrast difference between these two images is observed. It is because the X-ray films used in conventional cephalograms have the special nonlinear optical property that the characteristic curve between optical density and logarithmized X-ray exposure has a sigmoid-like shape [17]. According to the Lambert-Beer law, the logarithmized X-ray exposure is equivalent to the attenuation integral. It indicates that the intensity relation between the desired cephalogram and the attenuation integral image $\boldsymbol{g}$ should also exhibit a sigmoid-like curve. Therefore, to make the image

contrast of synthetic cephalograms similar to conventional cephalograms, a sigmoid intensity transform is necessary.

The standard sigmoid function is defined as the following,

$$\sigma(x) = 1/(1 + e^{-x}). \tag{3}$$

Considering shift, scaling and the intensity range [0, 255] in 8-bit gray scale images, the following general sigmoid function is proposed to transform the intensities of $\boldsymbol{g}$,

$$\tilde{\boldsymbol{g}}(y, z) = c_1 + (255 - c_1 - c_2)/\left(1 + e^{-s \cdot (\boldsymbol{g}(y,z)-t)}\right), \tag{4}$$

where c_1 is a base intensity value caused by film base attenuation and fog or unwanted exposure during storage and handling [17], c_2 is a parameter to decide the intensity saturation value, t is an intensity shift parameter, and s is a scaling factor for the slope of the curve. Since the standard sigmoid function has a value between 0 and 1, with the above sigmoid transform, $\tilde{g}$ has an intensity range of $[c_1, 255 - c_2]$.

To find the parameters for the above general sigmoid transform, the mean intensity values of samples chosen in certain regions of $\boldsymbol{g}$ together with the corresponding values sampled from real conventional cephalograms are plotted as black dots in Fig. 2(c). The sigmoid transform of Eqn. (4) is plotted as the red-dotted curve, whose parameters are determined by least squares curve fitting. As displayed, most samples are located near the sigmoid curve, which is consistent with the characteristic curve in X-ray films. Note that the positions of the samples are approximated very coarsely due to the absence of dental CBCT volumes and their corresponding cephalograms. With matching pairs, a more accurate intensity transform can be learned.

4) Modified sigmoid transform: With the original sigmoid transform, the air background and low intensity soft tissues both have values close to c_1. To recover air background, pixel values smaller than a threshold τ_1 in $\boldsymbol{g}$ are set to 0. In addition, to recover the contrast in soft tissues, for the low intensity range $[\tau_1, \tau_2]$, another sigmoid function is used,

$$\hat{\boldsymbol{g}}(y, z) = c_3 + c_4/\left(1 + e^{-(\boldsymbol{g}(y,z)-(\tau_1+\tau_2)/2)}\right), \tag{5}$$

where c_3 is a modified base intensity value and c_4 is an intensity parameter determined by setting $\hat{\boldsymbol{g}}(y, z) = \tilde{\boldsymbol{g}}(y, z)$ at $\boldsymbol{g}(y, z) = \tau_2$ for continuity. Here we choose a second sigmoid function instead of a linear function to make the curve smoother at the transition point $\boldsymbol{g}(y, z) = \tau_2$.

In summary, the final cephalogram $\boldsymbol{g}^*$ is obtained as

$$\boldsymbol{g}^*(y, z) = \begin{cases} 0, & \boldsymbol{g}(y,z) < \tau_1, \\ \hat{\boldsymbol{g}}(y, z), & \tau_1 \leq \boldsymbol{g}(y,z) \leq \tau_2, \\ \tilde{\boldsymbol{g}}(y, z), & \boldsymbol{g}(y,z) > \tau_2, \end{cases} \tag{6}$$

where the intensity transform is a modified sigmoid function, illustrated as the blue-dotted curve in Fig. 2.

B. Type II: Cephalogram Synthesis from 2D CBCT Projections

In this subsection, we propose a deep learning method to synthesize 2D cephalograms directly from 2D logarithmized projections for low-dose purpose. In order to train such deep learning models, it is optimal to have clinical dental CBCT projections and their corresponding conventional cephalograms as pairs. However, in practice, it is infeasible to obtain a sufficient number of such pairs due to ethic considerations, privacy concerns, and clinical regulations. For a proof of concept, we choose to use synthetic projection images from publicly available CBCT head data [44] as a surrogate in this work. The projections simulated based on a regular dental CBCT system configuration and the cephalograms synthesized by the above Type I method with orthogonal projection are used as pairs.

Dental CBCT systems typically have a shorter source-to-isocenter distance and a longer isocenter-to-detector distance than cephalometer systems. As a result, dental CBCT projections have more severe perspective deformations than conventional cephalograms, in addition to the image contrast difference. Therefore, the neural network needs to learn both the perspective deformation and the image contrast transform.

1) Neural network: For image-to-image translation, GANs are the state-of-the-art. Therefore, in this work, we propose to apply a pixel-to-pixel generative adversarial network (pix2pixGAN) [45] for cephalogram synthesis. The U-Net is used as the generator G while a 5-layer CNN is used as the discriminator D [45]. G learns to convert a cone-beam projection to a cephalogram. D learns to distinguish the synthetic cephalogram from the target cephalogram. The objective of the conditional GAN is,

$$\mathcal{L}_{\text{cGAN}}(G, D) = \mathbb{E}_{\boldsymbol{x}, \boldsymbol{y}}\left[\log D(\boldsymbol{x}, \boldsymbol{y})\right] + \mathbb{E}_{\boldsymbol{x}}\left[\log\left(1 - D(\boldsymbol{x}, G(\boldsymbol{x}))\right]\right., \tag{7}$$

where $\boldsymbol{x}$ is the input, $\boldsymbol{y}$ is the target, G tries to minimize this objective against an adversarial D that tries to maximize it, i.e., $G^* = \arg\min_G \max_D \mathcal{L}_{\text{cGAN}}(G, D)$. In addition, a weighted ℓ_1 loss function is applied to train the generator's output close to the target with less blurring compared to ℓ_2 loss,

$$\mathcal{L}_{\ell_1} = \mathbb{E}_{\boldsymbol{x}, \boldsymbol{y}}\left[||\boldsymbol{w} \cdot (\boldsymbol{y} - G(\boldsymbol{x}))||_1\right], \tag{8}$$

where $\boldsymbol{w}$ is a weight map calculated by the Sobel edge detector to emphasize edges [23].

2) Rebinning: In the CBCT system, we denote the source-to-isocenter distance by d_0 and the source-to-detector distance by d_1. Due to perspective projection, the anatomical structures at the midsagittal plane, which passes through the isocenter, have a magnification factor of d_1/d_0. To remove this magnification factor, the acquired CBCT projections are rebinned into a virtual detector (VD) located at the midsagittal plane. Such rebinning removes the magnification for structures in the midsagittal plane. However, structures in other sagittal planes still have different magnification factors, although these factors are reduced by rebinning. Therefore, the perspective deformation remains.

3) Patch selection: Cone-beam projections and cephalograms typically have a large image size. To avoid high computation burden, patch-wise learning is applied. In this work, the input of the generator G is a patch from a cone-beam projection while the target output is the corresponding patch from the paired cephalogram.

Note that due to perspective deformation the patch pairs need to be carefully selected. In the 3D patient volume, a 2D

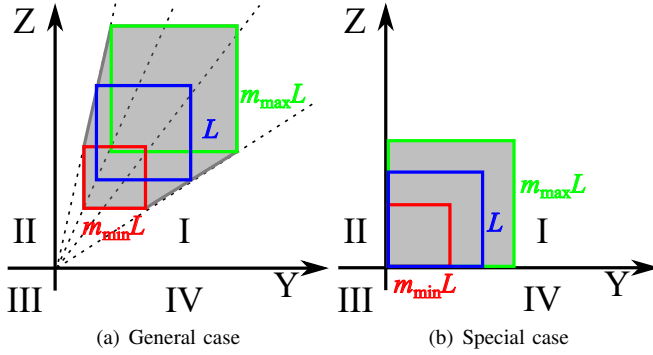(a) General case   (b) Special case

Fig. 3. The cone-beam projections of volume-domain patches on the VD. The blue square corresponds to the projected patch without any magnification, while the red square corresponds to the projected patch with the minimum magnification and the green square corresponds to the projected patch with the maximum magnification. The grey area corresponds to the union set of all the projected patches with different magnification factor between $m_{\min}$ and $m_{\max}$. (a) is a general case where the left bottom corners of the projected patches are inside the first quadrant, while (b) is a special case where the patch corners are located at origin.

square patch can be determined by its vertex location, edge length and orientation (direction of its normal vector). Here we consider patches all oriented along the X axis. Hence we can denote a 2D square patch with a left bottom vertex location (x, y, z) and an edge length L by $p_{\text{volume}}(x, y, z, L)$. Now we consider a set of parallel patches which share the same Y and Z coordinates, y_0 ($y_0 \geq 0$) and z_0 ($z_0 \geq 0$) respectively, for the left bottom vertexes and the same edge length L_0, while the X coordinate x can shift between $x_{\min}$ and $x_{\max}$. Such a patch is denoted by $p_{\text{volume}}(x, y_0, z_0, L_0)$, where $x_{\min} \leq x \leq x_{\max}$. In cone-beam projection, the anatomical structures in such a patch have a magnification factor of $m = d_0/(d_0 - x)$ in the VD. Hence, the projection of this patch has a corresponding left bottom corner vertex $(m \cdot y_0, m \cdot z_0)$ and an edge length $m \cdot L_0$. Since the magnification factor m varies between $m_{\max} = d_0/(d_0 - x_{\min})$ and $m_{\min} = d_0/(d_0 - x_{\max})$, the cone-beam projections of all the patches $p_{\text{volume}}(x, y_0, z_0, L_0)$, where $x_{\min} \leq x \leq x_{\max}$, are located in a hexagon, as displayed in the grey area in Fig. 3(a). However, the orthogonal projections of all the patches $p_{\text{volume}}(x, y_0, z_0, L_0)$, where $x_{\min} \leq x \leq x_{\max}$, are located in a square patch with the corresponding left bottom vertex (y_0, z_0) and the edge length L_0, as displayed in the blue square in Fig. 3(a). Therefore, it is difficult to find exact matching patch pairs in the general case for such a hexagon-to-square mapping.

However, in the special case of $y_0 = 0$ and $z_0 = 0$, this hexagon area becomes a square, as displayed in Fig. 3(b). But the grey square area and the blue square area in Fig. 3(b) have different edge lengths. This issue can be relieved by choosing a large patch size L, e.g., each patch being one quadrant, so that the area between the blue square and the grey square has zero values since human heads are compact. Accordingly, in this work, we divide each CBCT projection into four patches according to the four quadrants.

4) One model for multi-quadrant patches: The perspective deformation is inhomogeneous. For the patches in the first quadrant, the anatomical structures near the left bottom corner
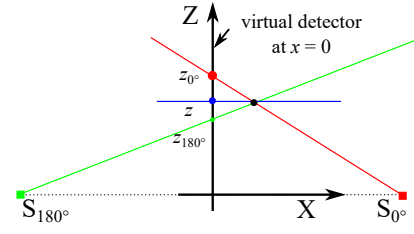

Fig. 4. The benefit of dual projections in localizing anatomical structures in cone-beam projections visualized in the X-Z plane. The VD is located in the plane of $x = 0$. The cone-beam projections (the red and green points) of the black point (x, y, z) from the $0°$ and $180°$ X-ray sources to the VD have the heights of $z_{0°}$ and $z_{180°}$ respectively, while its orthogonal projection (the blue point) has the height of z with the relation $z_{0°} < z < z_{180°}$ in this example.

have the minimum deformation while those near the right top corner have the most deformation. However, for the patches in the second quadrant, the anatomical structures near the right bottom corner have the minimum deformation while those near the left top corner have the most deformation. Therefore, for each quadrant an individual model needs to be trained due to different perspective deformation patterns. However, it is likely that the four models will learn (or rather "memorize") quadrant-specific features, which may be not related to perspective deformation. To mitigate this problem and to reduce the computation burden of training four models as well, the symmetry property is utilized. If the patches from the second quadrant are flipped horizontally, then the patches have the same perspective deformation as those from the first quadrant. Similarly, we can apply horizontal + vertical flipping and vertical flipping respectively for the patches from the third and the fourth quadrants to get the same deformation pattern. With such flipping operations, all the patches from different quadrants can be used together to train one model. Such a model is expected to learn the common features in these four-quadrant patches, i.e. perspective deformation, instead of quadrant-specific features.

5) Dual projections to one cephalogram synthesis: In orthogonal projection, if the parallel-beam rays are rotated by $180°$, the acquired projection is the same as the original projection after a horizontal flip. Therefore, in parallel-to-cone projection conversion, using an additional $180°$ projection is entirely redundant. However, in cone-to-parallel projection conversion in this work, $180°$ projections can provide additional information together with $0°$ projections due to the following two factors: a) The isocenter (or rotation axis) of a dental CBCT system is not perfectly locate at the midsagittal plane of a head; b) Human heads are not perfectly symmetric with respect to (w. r. t.) the midsagittal plane. Therefore, using dual projections is beneficial in localizing anatomical structures with perspective deformation. To illustrate this benefit, a sketch of the dual cone-beam projections of a point visualized in the X-Z plane is displayed in Fig. 4. The cone-beam projections (the red and green points) of the black point (x, y, z) from the $0°$ and $180°$ X-ray sources to the VD (located at the Y-Z plane with $x = 0$) have the heights of $z_{0°}$ and $z_{180°}$, respectively, while the orthogonal projection (the blue point) of the black point has the height of z. It is clear that the value of z

(a) 0° rebinned CBCT projection   (b) 180° rebinned CBCT projection
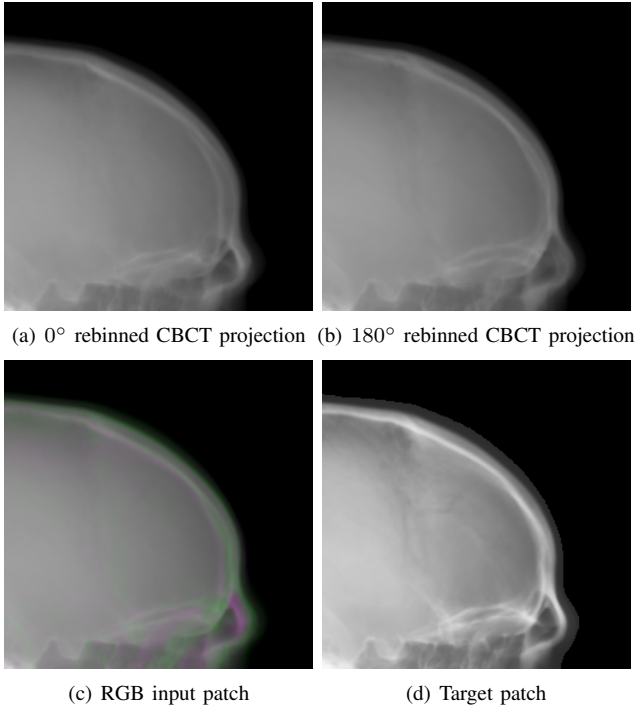

(c) RGB input patch   (d) Target patch

Fig. 5. One patch example for dual projections to one cephalogram synthesis: (a) the first quadrant patch from the 0° cone-beam projection; (b) the first quadrant patch (horizontally flipped) from the 180° cone-beam projection; (c) the RGB patch using (a) for the red and blue channel and (b) for the green channels, where the colourful area highlight the difference between (a) and (b); (d) the target patch synthesized by our proposed volume-to-cephalogram method.

is between $z_{0°}$ and $z_{180°}$, if the point is not located in the plane of $x = 0$. This relation indicates that the orthogonal projection of an anatomical structure must be between the locations of its 0° and 180° cone-beam projections.

It is worth noting that using projections other than the 0° and 180° projections, e.g. 1° or 90°, will introduce additional deformation caused by angular rotations. Therefore, only 0° and 180° these two angles are chosen.

To combine such dual projection information, we convert the patches from 0° and 180° cone-beam projections to 3-channel patches forming RGB color patches. The 0° patch is used for the red channel and blue channel, while the 180° patch is used for the green channel. The 0° patch instead of the 180° patch takes two channels, since the target cephalograms are also acquired in the 0° view in our setting. In the RGB patch, the intensity difference between the 0° patch and the 180° patch is revealed by the color: Grey areas have the same values for the three channels, indicating that the intensity values from the 0° and 180° patches respectively are close to each other, while green areas indicate that the 180° patch has larger values and magenta areas indicate that the 0° patch has larger values. An example is displayed in Fig. 5, where Figs. 5(a) and (b) are the 0° and 180° patches respectively, Fig. 5(c) is the RGB patch as the input of the neural network, and Fig. 5(d) is the corresponding target output of the neural network.

C. Super Resolution

In dental CBCT systems, the flat-panel detectors typically have a resolution around 0.3 mm/pixel. Due to the pursue of fast reconstruction, typically the 3D volume resolution is around 0.5 mm/pixel [18]. In contrast, the image resolution in conventional film-based cephalograms is as high as 0.1 mm/pixel. Therefore, image resolution in synthetic cephalograms is worse than that in real cephalograms in general. To reduce blur in synthetic cephalograms, deep learning SR techniques are applied.
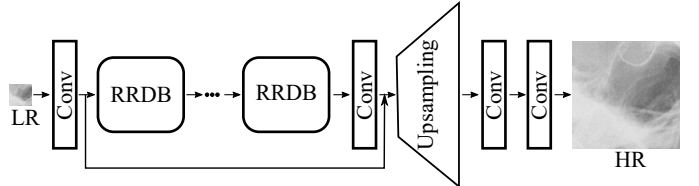

Fig. 6. The architecture of the generator in ESRGAN$_{RRDB}$ [34].

In this work, we investigate the application of two ESR-GANs [33], [34] for SR in this work. For distinction, we refer to [33] as ESRGAN$_{RDB}$ and [34] as ESRGAN$_{RRDB}$ respectively, as they utilize RDBs and RRDBs respectively for the basic blocks in the generator. The architecture of the generator in ESRGAN$_{RRDB}$ is displayed in Fig. 6 as an example. Since in this work the scaling factor from LR to HR images is large, 0.5 mm/pixel to 0.1 mm/pixel particularly, checkerboard artifacts [46] are observed in predicted HR images, although the PixShuffle or deconvolution operation is replaced by upsampling followed by a convolution [46]. Therefore, similar to SRCNN [27], we choose to use ILR images using bicubic upsampling as the input of the generator along with the removal of the upsampling layer, which effectively reduces checkerboard artifacts. Additional information on network architecture, loss function and training procedure for the ESRGANs are provided in the original publications [33] and [34], respectively. In addition, the U-Net has been demonstrated effective for SR in dental imaging [19]. Therefore, pix2pixGAN using the U-Net generator is also investigated to map ILR images to HR images. Note that the SR task uses an individual neural network because it allows us to train with very small patches. If it is included in the pix2pixGAN for Type II synthesis, very large patches (in our experiments, 1280×1280) need to be used, which is very computationally expensive.

D. Automated Cephalometric Landmark Detection

For cephalometric landmark detection, we propose a fully automated deep learning method combining LeNet-5 [47] and ResNet50 [43]. Our method is an improved version of the latest landmark detection method [42] in terms of efficiency. In [42], the ResNet50 is used to detect the location of one landmark in each ROI patch. To obtain the ROI patches, registering a test image to 150 training images to find the closet reference image is necessary. However, this registration step is computationally expensive and can take up to 20 minutes [42]. Therefore, we propose to utilize another neural network to
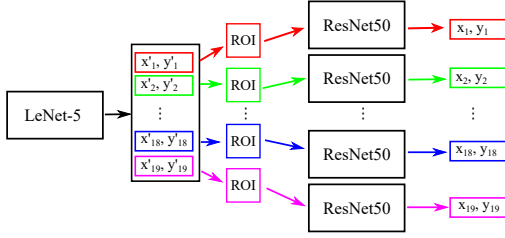
Fig. 7. The combination of LeNet-5 and ResNet50 for cephalometric landmark detection, where LeNet-5 approximately determines the ROI patches of 19 landmarks and each ResNet50 further determines the final location of each landmark.

determine the region which ResNet50 should pay attention to. In this work, we choose the LeNet-5 [48] to obtain such ROI patches. LeNet-5 has a simple architecture, which is efficient and stable for training. Although LeNet-5 is not sufficient to detect the 19 landmarks accurately, it is sufficient to detect a ROI patch for a subsequent neural network to work on.

The whole neural network architecture is displayed in Fig. 7. The output of the LeNet-5 is a 1-dimensional vector of 38 elements, representing the 38 coordinate candidates of the 19 landmarks. For the ith landmark, the predicted position is denoted by (x'_i, y'_i). Each position determines a ROI patch with a size of 512×512 pixels centred at (x'_i, y'_i) in the HR cephalogram image. The large patch size also relieves the accuracy demand on the LeNet-5. For each ROI patch, a ResNet50 model is trained respectively to predict the accurate position of the corresponding landmark. The final predicted position of each landmark is denoted by (x_i, y_i) for the ith landmark. Here we train 19 different ResNet50 models instead of training one model to predict 19 landmarks simultaneous, as landmark specific features can be extracted by each ResNet50 to achieve higher accuracy.

E. Experimental Setup

The proposed methods are demonstrated on the CQ500 head CT dataset [44]. It consists of 491 scans, whereby 5 complete head scans are used for testing purposes.

1) Parameters for Type I cephalogram synthesis: For skeleton enhancement, the weight a in Eqn. (1) is 1.3 as aforementioned. For sigmoid transform in Eqn. (4), the base intensity value c_1 is 40 and the saturation parameter c_2 is 5, the intensity shift parameter t is 2.6, and the scaling factor s is 1.5. For the modified sigmoid transform, c_3 and c_4 are 18 and 23, respectively. The thresholding parameter τ_1 and τ_2 are 0.1 and 1.2, respectively. The synthetic cephalograms $\boldsymbol{g}^*$ have an image size of 512×512 with a pixel resolution of $0.5\,\text{mm} \times 0.5\,\text{mm}$.

2) Parameters for Type II cephalogram synthesis: The CBCT projections are simulated using a ray driven method with a sampling rate of 3/mm. The source-to-isocenter distance and the source-to-detector distance of the CBCT system are 950 mm and 650 mm, respectively. Dental CBCT systems use flat panel detectors typically with a pixel size up to 0.1 mm. To save computation time, in this work the detector has 512×512 rebinned pixels with a pixel resolution of $0.73\,\text{mm} \times 0.73\,\text{mm}$. The $180°$ projections are horizontally flipped to have the

same orientation as the $0°$ projections. Afterwards, both the $0°$ and $180°$ projections are rebinned to the VD located at the isocenter to reduce magnification. As a result, the rebinned projections have an image size of 512×512 with a pixel resolution of $0.5\,\text{mm} \times 0.5\,\text{mm}$. Note that finer resolution is typically available in practice. In this work, we choose $0.5\,\text{mm} \times 0.5\,\text{mm}$ so that we can reuse the same SR models from Type I synthesis. The rebinned projections are further divided to four patches with a patch size of 256×256 according to the four quadrants. The patches from the other quadrants are flipped horizontally or vertically to have the same perspective deformation as those from the first quadrant. Afterwards, the patches are converted to RGB patches as the input of the neural network, where the intensity range [0, 6] is linearly mapped to [0, 255]. In total, 1840 patches are generated. Among them, 1600 patches are used for training, 40 patches for validation, and 200 patches for test. For training, 300 epochs with the Adam optimizer are used. The initial learning rate is 0.0002 with a decay rate of 0.999. The weight for the ℓ_1 loss is 100.

3) Parameters for super resolution: The SR models are trained on the ISBI Challenge training dataset [35], [36]. The original cephalograms have an image size of 1935×2400 with a pixel resolution of $0.1\,\text{mm} \times 0.1\,\text{mm}$. The original cephalograms are down-sampled with a factor of 5 using averaging down-sampling to have an image size of 387×480 with a pixel resolution of $0.5\,\text{mm} \times 0.5\,\text{mm}$. In addition, the original cephalograms are also down-sampled with a factor of 10 and further up-sampled with a factor of 2. The resulted images also have a pixel resolution of $0.5\,\text{mm} \times 0.5\,\text{mm}$, but with more blurry structures. This operation is carried out to have different levels of blur in the training images, since our test images from the CQ500 dataset are acquired from different CT scanners, leading to different resolutions. For SR models using ILR images as the input, the LR images are up-sampled with a factor of 5 using bicubic up-sampling to have a pixel resolution of $0.1\,\text{mm} \times 0.1\,\text{mm}$. The LR patches have an image size of 64×64, while the ILR and HR patches have an image size of 320×320. For each cephalogram among the ISBI datasets, we generate 42 patches. In total, we have 6300 patches for training, 420 patches for validation, and 2100 patches for test. For each method, 100 epochs are used for training with the Adam optimizer. For pix2pixGAN in the SR task, no weight is applied for the ℓ_1 loss, i.e., $\boldsymbol{w} = \mathbf{1}$ in Eqn. (8).

4) Parameters for landmark detection: We train the proposed network in two steps, one for the LeNet-5 and the other for the ResNet50. For the LeNet-5 part, the 150 down-sampled images from the ISBI training dataset and the corresponding given landmark locations are used for training. The loss function is mean absolute error (MAE). The Adam optimizer is used. The initial learning rate is 0.1 with a decay rate of 0.999. In total, 50 epochs are used for training. For the ResNet50 part, a 512×512 patch is generated for each given landmark position. The detected landmark is located at the center of the corresponding patch. The patches are rotated by $90°$, $180°$ and $270°$ as data augmentation. Overall, 60000 patches are used for training each model. 19 models are trained for the 19 landmarks respectively. MAE is used as the loss function
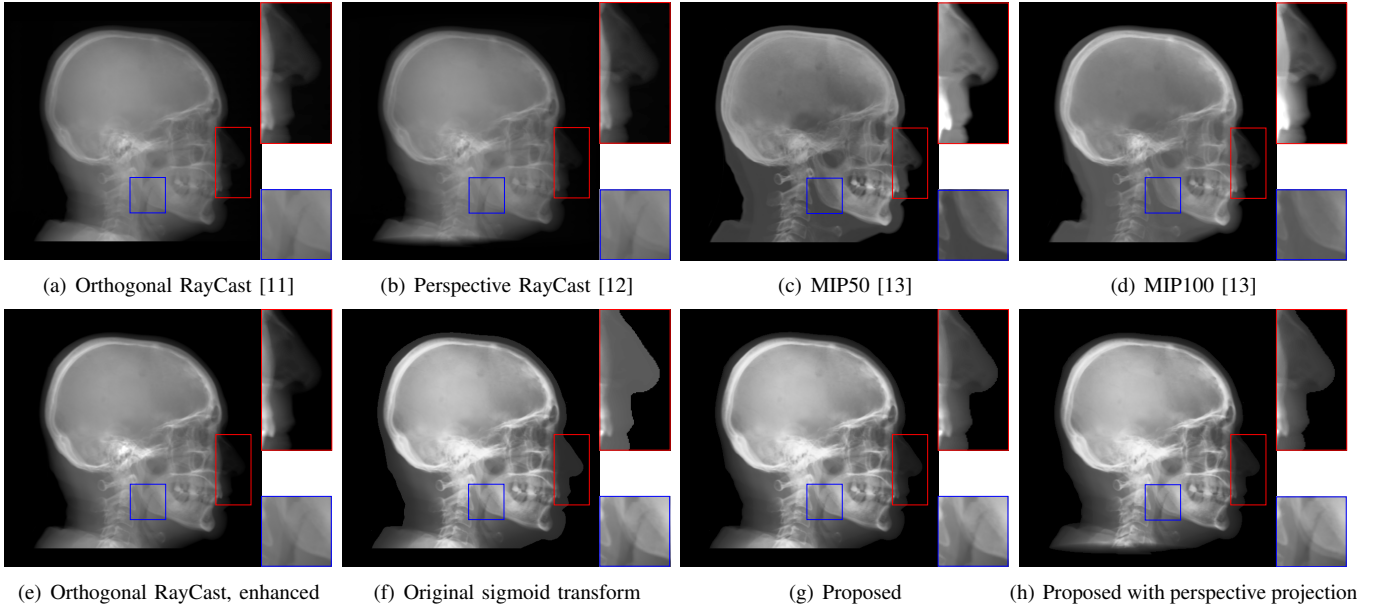
Fig. 8. Synthetic cephalogram examples from 3D CBCT volumes with different methods. (a)-(d) are comparison results while (e)-(h) are the (intermediate) results of our proposed method: (a) RayCast using orthogonal projection; (b) RayCast using perspective projection; (c) MIP using the largest 50 pixels along each orthogonal ray; (d) MIP using the largest 100 pixels along each orthogonal ray; (e) RayCast using orthogonal projection from the skeleton enhanced volume; (f) original sigmoid transform of (e) using Eqn. (4) with air background recovery; (g) modified sigmoid transform of (e) using Eqn. (6), the final Type I synthetic cephalogram using orthogonal projection; (h) final Type I synthetic cephalogram using perspective projection. The nose ROIs are redisplayed in the intensity window [0, 125] for better visualization. The mandible angle ROIs are for the visualization of the difference between orthogonal projection and perspective projection.

and the Adam optimizer is used. The initial learning rate is 0.1 with a decay rate of 0.999. In total, 50 epochs are used for training. Due to the large amount of training data, in every 10 epochs, 6000 patches are randomly chosen for training.

IV. RESULTS

A. Results of Type I Cephalogram Synthesis

The synthetic cephalograms generated by different methods are displayed in Fig. 8. Figs. 8(a) and (b) show the cephalograms synthesized by the orthogonal [11] and perspective [12] RayCast methods, respectively, which are the most widely used methods for cephalogram synthesis from CBCT volumes. In Fig. 8(a), anatomical structures on both sides of the midsaggital plane overlap well in the orthogonal projection. In contrast, due to different magnification factors of structures at different positions in perspective projection, anatomical structures on both sides of the midsaggital plane cannot overlap exactly, for example, the projections of the left and right mandible (gonial) angles in the zoom-in ROI in Fig. 8(b). In Figs. 8(a) and (b), the skeleton structures, soft tissues and airways are well observed. However, the image contrast in these two synthetic cephalograms are different from conventional cephalograms (Fig. 2(a)). The cephalograms synthesized by MIP using the largest 50 pixels and 100 pixels along each orthogonal ray are displayed in Figs. 8(c) and (d), respectively. In both images, skeleton structures are well observed since they have high intensities. Comparing Fig. 8(d) to (c), more anatomical details are added. Nevertheless, in both images, low intensity structures, e.g. the throat airway, might disappear.

Figure 8(e)-(g) are the Type I synthetic cephalograms of different steps using orthogonal projection. Fig 8(e) is the orthogonal RayCast celphalogram synthesized from the enhanced CBCT volume using Eqn. (1). Compared with Fig 8(a), skeleton structures in Fig 8(e) have higher contrast. Fig 8(f) is the obtained by applying the original sigmoid transform in Eqn. (4) to Fig 8(e), where the skeleton structures are further enhanced. Moreover, the appearance of Fig 8(f) is very close to conventional cephalograms. However, the soft tissues like the nose and lips have an almost constant intensity value, as displayed in the zoom-in ROI in Fig 8(f). The final Type I synthetic cephalogram with orthogonal projection is displayed in Fig 8(g). With the proposed modified sigmoid transform in Eqn. (6), the contrast in the soft tissues is brought back, as displayed in the zoom-in ROI. For comparison, the final Type I synthetic cephalogram with perspective projection is displayed in Fig 8(h).

B. Results of Type II Cephalogram Synthesis

The cephalogram synthesis results of two patches and one complete stitched cephalogram image are displayed in Fig. 9. In the top row, the blue curve is the outline of the target patch, while the red and green curves are the outlines for the $0°$ and $180°$ projections, respectively. Consistent with the relationship in Fig. 4, the blue curve is between the red and green curves. Since the $180°$ projection (green channel) has larger area than the $0°$ projection (red and blue channels), the region near the boundary appears green in the RGB input patch in Fig. 9(c). Fig. 9(d) is the target output. Fig. 9(e) is the output using the $0°$ projection only, where the outline has large deviation from the target blue curve. In contrast, in Fig. 9(f)

| 0° projection | 180° projection | RGB projection | Target | 1-projection output | 2-projection output |

(a) | (b) | (c) | (d) | (e) 13.56, 24.66 | (f) 6.98, 30.26

(g) | (h) | (i) | (j) | (k) 5.35, 32.43 | (l) 4.12, 34.70

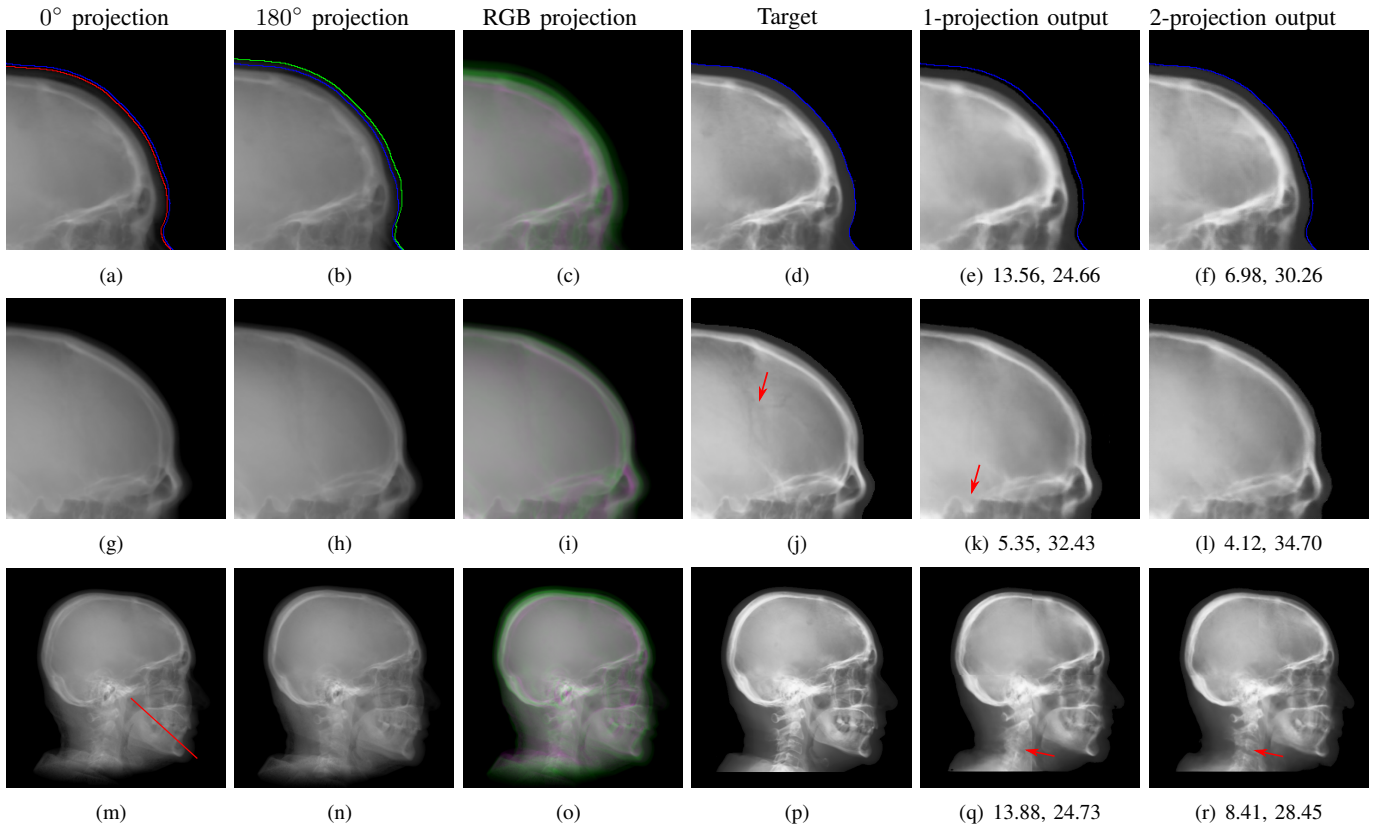(m) | (n) | (o) | (p) | (q) 13.88, 24.73 | (r) 8.41, 28.45

Fig. 9. Synthetic cephalogram examples from 2D CBCT projections. The top two rows are two patches respectively while the bottom row is a complete stitched cephalogram. In the top row, the blue curve is the outline of the target patch, while the red and green curves are the outlines for the 0° and 180° projections, respectively. In the middle row, the cranial sutures indicated by the arrow in (j) are not visible in (k) nor in (l); the sella turcica indicated by the arrow in (k) is distorted. In the bottom row, the vertebrae indicated by the arrow in (r) are more accurate than those in (q). The line in (m) mark the position for line profiles in Fig. 10. For the 1-projection output and 2-projection output, the RMSE (left) and PSNR (right) values w. r. t. the target are displayed in the corresponding subcaptions.
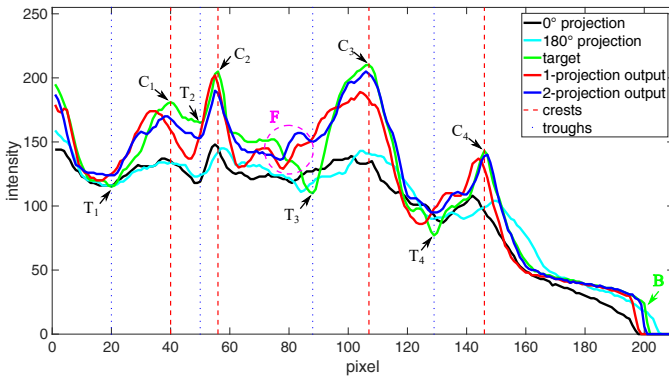

Fig. 10. Intensity profiles of a chosen line a chosen line from Figs. 9(m)-(r). The position of the line is marked in Fig. 9(m). The boundary area is marked by B. The major crests and troughs in the target curve are marked as C_i and T_i where $i = 1, 2, 3, 4$, respectively, while a circular region near T_3 contains small crests and troughs is marked by F.

where the dual projections are used, the outline is closer to the target blue curve. In the middle row, the sella turcica in the 1-projection output has large distortion, as indicated by the arrow in Fig. 9(k), compared with that in the target patch. On the contrary, the sella turcica in the 2-projection output (Fig. 9(l)) preserves its shape. These observations highly demonstrate the benefit of using dual projections.

In the bottom row, the results of one complete cephalogram are displayed. Compared with Fig. 9(q), some structures like the vertebrae indicated by the arrow in Fig. 9(r) are more accurate. For quantification, the intensity profiles of a chosen line from Figs. 9(m)-(r), the position of which is marked in Fig. 9(m), are plotted in Fig. 10. For the boundary area marked by B, the profile of 2-projection output is the most closest one to the target profile compared with others, which is consistent with the results in Fig. 9(a)-(f). The major crests and troughs in the target curve are marked as C_i and T_i where $i = 1, 2, 3, 4$, respectively, while a circular region near T_3 contains small crests and troughs is marked by F. The intensity differences between crests and troughs in the target profile and the 2-projection output profile, as well as the 1-projection output profile, are larger than those in the 0° and 180° projections, indicating image contrast improvement in our synthetic cephalograms. In the F region, the 2-projection output profile, as well as the 1-projection output file, has deviation from the target profile. Nevertheless, all other major crests and troughs in the 2-projection output profile are concurrent with those of the target profile. Compared with those of the 1-projection output, the crest and trough positions of the 2-projection output are more accurate, especially for C_1, C_4, T_2, and T_4. This highlights the benefit of using dual projections in learning perspective deformation.

TABLE I
QUANTITATIVE EVALUATION OF DIFFERENT METHODS FOR
CEPHALOGRAM SYNTHESIS FROM 2D CBCT PROJECTIONS.

Method	one projection, one model	dual projections, one model	dual projections, four models
RMSE	10.04	5.47	5.01
PSNR	28.03	33.10	33.83

The average RMSE and PSNR values of all the test patches is displayed in Tab. I. Using one model for four quadrants with one projection as the input of the pix2pixGAN, the average RMSE and PSNR values are 10.04 and 28.03 respectively. Using one model for four quadrants with dual projections, the image quality of synthetic cephalograms is significantly improved with RMSE = 5.47 and PSNR = 33.10. Therefore, using dual-projection RGB patches for training is superior to using one-projection only. While using four models for four respective quadrants with dual projections, the average RMSE and PSNR values are slightly improved without significance. Hence, using one model for four quadrant patches is applicable according to the symmetry property of perspective deformation.

C. Results of Super Resolution

The SR results on the test patches of the ISBI Test1 data are displayed in Fig. 11. Compared with the reference patches, the bicubic interpolation patches have blurry structures. Especially, the skeleton edges in Fig. 11(b) suffer from jagging artifacts due to the large sampling scale. The structures in the outputs of ESRGAN$_{RDB}$ and ESRGAN$_{RRDB}$ using LR patches as the input have sharp edges. However, a certain level of checkerboard artifacts are observed. In the results of ESRGAN$_{RDB}$ and ESRGAN$_{RRDB}$ using ILR patches (i.e., the bicubic interpolation patches displayed in Figs. 11(b) and (i)) as the input, jagging artifacts remain in the edges. In the results of pix2pixGAN, high resolution structures are recovered without the introduction of jagging nor checkerboard artifacts. The quantitative evaluation results on all the test patches in Tab. II also indicate that pix2pixGAN achieves the best image quality, achieving the best RMSE of 4.8 and PSNR of 32.5.

TABLE II
THE QUANTITATIVE EVALUATION OF DIFFERENT SR METHODS ON THE
ISBI TEST1 DATA.

Methods	RDB LR	RDB ILR	RRDB LR	RRDB ILR	pix2pixGAN
RMSE	16.8	9.7	10.0	8.5	4.8
PSNR	22.4	27.2	26.5	28.0	32.5

The SR techniques are also applied to synthetic cephalograms. The results of one Type I synthetic cephalogram example are displayed in Fig. 12. To visualize details better, an ROI patch is chosen for each method, whose position is marked in Fig. 12(a). Consistent with the results on the ISBI test patches, the patches of ESRGAN$_{RDB}$ and ESRGAN$_{RRDB}$ using LR patches as the input also suffer from checkerboard artifacts in Figs. 12(h) and (j). In addition, some undesired bright/dark artifacts occurs in Fig. 12(j). In Figs. 12(i) and (k), apparent

jagging artifacts are no longer observed for ESRGAN$_{RDB}$ and ESRGAN$_{RRDB}$ using ILR patches as the input, since the edges in the bicubic interpolation patches are smooth without jaggies. Nevertheless, the soft tissues like the nose have lower intensity in Fig. 12(c) than those in Fig. 12(a). As expected, the patch predicted by pix2pixGAN has realistic appearance without the introduction of jagging nor checkerboard artifacts. Due to its superior performance to ESRGAN$_{RRDB}$ using ILR on the ISBI test patches, in this work we choose pix2pixGAN as the SR method.

D. Results of Landmark Detection

To validate the efficacy of our proposed automatic landmark detection algorithm, it is compared with other state-of-the-art algorithms on the benchmark ISBI data (Testset1 and Testset2). The SDRs of different algorithms [37]–[42] in different precision ranges for Testset1 and Testset2 are displayed in Fig. 13(a) and (b), respectively. Our proposed method achieves the 2 mm-SDRs of 86.7% and 73.7% on the ISBI Testset1 and Testset2, respectively, which is comparable to the best accuracy methods [41], [42]. However, our method is more efficient than [41] and has a simpler architecture than [42].

Our proposed landmark detection method is applied to detect landmarks in synthetic cephalograms. The results of three example patients are displayed in Fig. 14. Cephalograms in the top row are obtained by different synthesis methods from 3D volumes for the first patient. The mid and bottom rows are Type I and Type II synthetic cephalograms, respectively. The green and blue labels are manual detection landmark positions in Type I and Type II synthetic cephalograms respectively, while the red labels are automated detection landmark positions in each cephalogram. The green labels are used as the reference. The overall SDRs of the landmarks in different types of synthetic cephalograms on the test patients are displayed in Tab. III. The last row SDRs are calculated from manual detection (blue) landmarks in Type II synthetic cephalograms w. r. t. reference landmarks, while others are from automatic detection (red) landmarks w. r. t. reference landmarks.

For RayCast in Fig. 14(a), many automatic detection landmarks exceed the 4 mm precision range such as the landmarks of anterior nasal spine, gonion, porion and articulare. According to Tab. III, overall only 45.6% landmarks are detected within the 4 mm precision range by the automatic landmark detection algorithm. For MIP100 in Fig. 14(b), the landmarks of sella, porion, articulare have very large deviations from the reference landmarks. Overall, it achieves 47.4% 2 mm-SDR and 81.5% 4 mm-SDR. Figs. 14(c) and (d) are the cephalograms synthesized by our Type I synthesis with the original sigmoid transform and the modified sigmoid transform, respectively. These two synthetic cephalograms have subtle difference in the soft-tissue areas. As a result, the detected incision superius and lower lip positions exceed the 4 mm range in Fig. 14(c) while they are well detected within the 2 mm precision range in Fig. 14(d). This demonstrates the benefit of the modified sigmoid transform.

For Type I synthesis, two more cephalograms are displayed in Figs. 14(e) and (f). Overall, 93.0% automatic detection
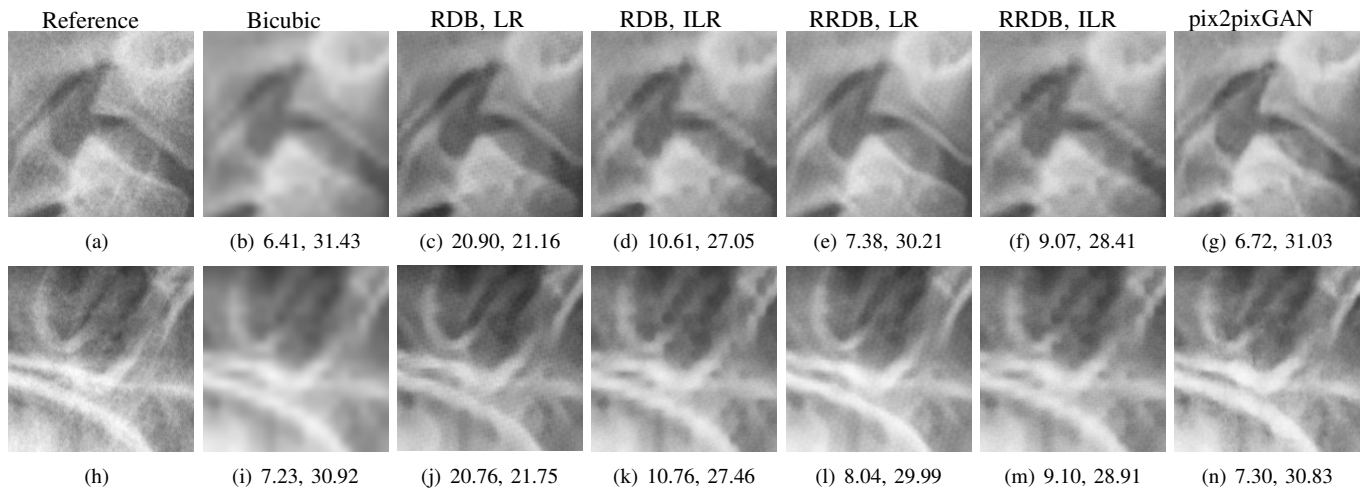
Reference	Bicubic	RDB, LR	RDB, ILR	RRDB, LR	RRDB, ILR	pix2pixGAN

| (a) | (b) 6.41, 31.43 | (c) 20.90, 21.16 | (d) 10.61, 27.05 | (e) 7.38, 30.21 | (f) 9.07, 28.41 | (g) 6.72, 31.03 |

| (h) | (i) 7.23, 30.92 | (j) 20.76, 21.75 | (k) 10.76, 27.46 | (l) 8.04, 29.99 | (m) 9.10, 28.91 | (n) 7.30, 30.83 |

Fig. 11. SR test examples on the ISBI Test1 data. The RMSE (left) and PSNR (right) values are displayed in the corresponding subcaptions.

Bicubic	RDB, LR	RDB, ILR	RRDB, LR	RRDB, ILR	pix2pixGAN

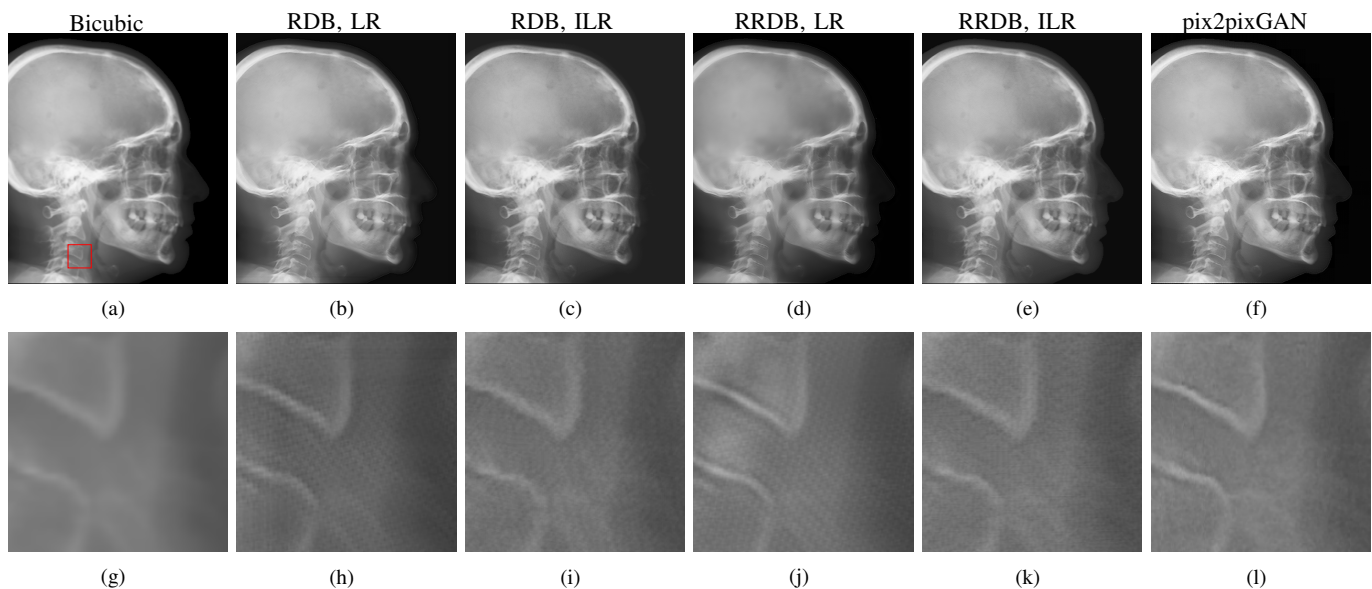| (a) | (b) | (c) | (d) | (e) | (f) |

| (g) | (h) | (i) | (j) | (k) | (l) |

Fig. 12. Ssuper r results on synthesized cephalogram from 3D volumes. The position of the example ROI patches in the bottom row is marked in (a).

landmarks are overlapped with the reference landmarks within the precision range of 4 mm, with a few exceptions such as the sella landmark in (d), the porion in (e), and the incision inferius and subnasale landmarks in (f) beyond 4 mm. Particularly, 75.4% automatic detection landmarks are within the 2 mm clinical acceptable precision range. This indicates that the automatic landmark detection algorithms learned from real conventional cephalograms can be applied to our Type I synthetic cephalograms.

For Type II synthetic cephalograms in Figs. 14(d)-(f), all the manual detection (blue) landmarks are overlapped with the reference landmarks within the distance range of 4 mm, indicating that the landmark positions in the Type II synthetic cephalograms have no impactful position shift from those in Type I synthetic cephalograms. The majority (80.7%) of the automatic detection (red) landmarks are also overlapped with the reference landmarks within the 4 mm precision range. However, more automatic detection landmarks in Type II

synthetic cephalograms are outside the 4 mm range than those in Type I synthetic cephalograms, for example, the anterior nasal spine landmark in (d), the orbitale landmark in (e), the incision inferius landmark in (f), the nasion landmarks in (e) and (f), and the gonion landmarks in (d)-(f). The 2 mm-SDR also decreases from 75.4% to 50.9%.

TABLE III
SDRs FOR 2.0 MM, 2.5 MM, 3.0 MM AND 4.0 MM PRECISION RANGES.

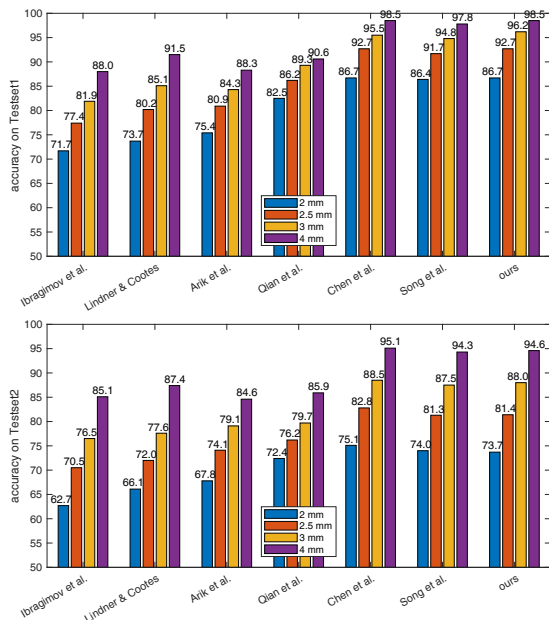| Point-to-point pairs	2 mm	2.5 mm	3 mm	4mm
RayCast (auto)	31.6	38.6	38.6	45.6
MIP100 (auto)	47.4	59.6	70.2	81.5
Original sigmoid (auto)	49.1	63.1	73.7	84.2
Type I (auto)	75.4	82.5	84.2	93.0
Type II (auto)	50.9	64.9	68.4	80.7
Type II (manual)	73.7	87.7	91.2	100

Fig. 13. Accuracy comparison of different cephalometric landmark detection algorithms [37]–[42] on ISBI Testset1 and Testset2.
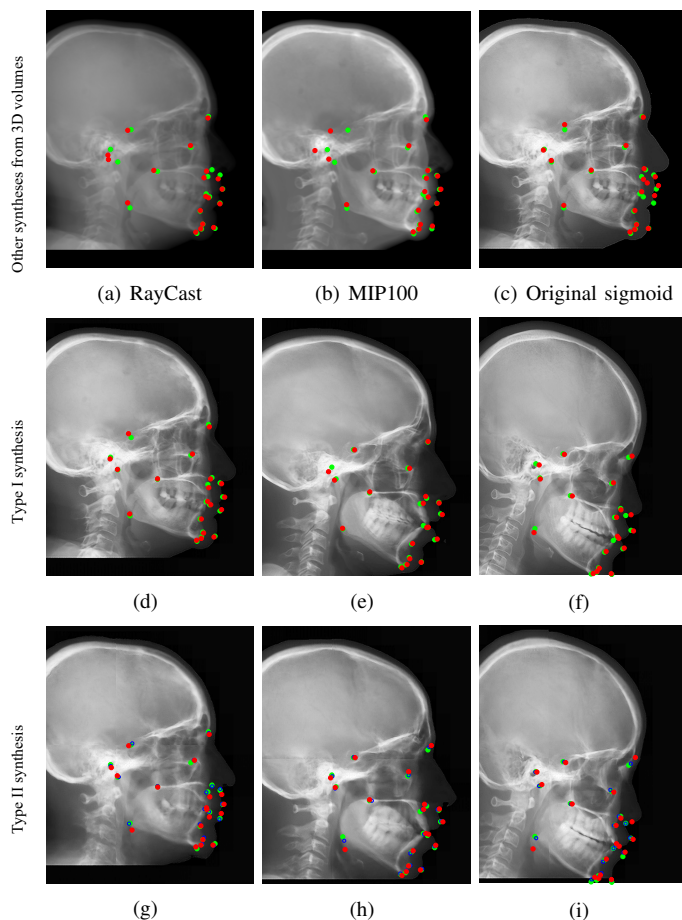

Fig. 14. Landmark detection on synthetic cephalograms. Cephalograms in the top row are obtained by different synthesis methods from 3D volumes for the first patient (the same patient for (d) and (g)). The middle and bottom rows are Type I and Type II synthetic cephalograms respectively from three example patients. The green (reference) and blue labels are manual detection landmark positions in Type I and Type II synthetic cephalograms respectively, while the red labels are automated detection landmark positions in each cephalogram.

V. DISCUSSION

The accuracy of landmarks in synthetic cephalograms using RayCast from 3D CBCT volumes has been validated in previous research [9]–[11]. Our Type I cephalogram synthesis method is an improved version of RayCast. Therefore, the accuracy of landmarks in our Type I synthetic cephalograms is guaranteed in principle. The improvement lies in image contrast based on the optical properties of conventional X-ray films and image resolution using SR techniques, making synthetic cephalograms closer to real conventional cephalograms. With the above premises, using the Type I synthetic cephalograms as the target of cephalogram synthesis from 2D projections has practical value.

In our Type II cephalogram synthesis, pix2pixGAN is capable to improve image contrast and reduce the perspective deformation, as demonstrated in Fig. 9 and Fig. 10. Therefore, using synthetic cephalograms from 2D projections for cephalometric analysis is promising. But it is worth noting that some information, especially for low contrast high frequency structures, is missing or incorrect in the Type II synthetic cephalograms compared with Type I synthetic cephalograms. For example, in Fig. 9(j) the cranial sutures indicated by the arrow are visualized. However, in the 2D projections in Figs. 9(g)-(i), they are barely seen. As a result, they are not visible in the output of pix2pixGAN, no matter using one projection or dual projections as the input. Another example is the circular region marked by F in Fig. 10. Nevertheless, dominant structures are preserved, as highlighted by the positions of the major crests and troughs in our dual-projection output in Fig. 10. These structures guarantee the accuracy of manual landmark identification, as demonstrated by Fig. 14 and Tab. III where all the manual detection landmarks in Type I and Type II cephalograms are within the 4 mm precision range.

With the existing database of conventional cephalograms, automatic cephalometric landmark detection algorithms are developed. In order to transfer these algorithms to synthetic cephalograms, the synthetic cephalograms should share as many features as possible with conventional cephalograms to get high detection accuracy. Due to the low image contrast in RayCast synthetic cephalograms, the SDRs are low, as displayed in Tab. III. Image contrast is improved in MIP100 synthetic cephalograms. Therefore, the 4 mm-SDR increases from 45.6% to 81.5%. With our proposed Type I synthesis method, the synthetic cephalograms are close to conventional cephalograms in terms of image contrast and resolution. Meanwhile, all anatomical structures including low intensity ones are contained in Type I synthetic cephalograms compared with MIP100 synthetic cephalograms. Therefore, the highest 2 mm-SDR is achieved in Type I synthetic cephalograms. It demonstrates that the landmark detection model learned from the ISBI dataset is applicable for landmark detection in our Type I synthetic cephalograms.

Compared with the synthetic cephalograms with the original sigmoid transform, those with our proposed modified sigmoid transform have only subtle difference in image contrast for the soft-tissues. However, such subtle difference substantially affects the automatic landmark detection, as shown in Tab. III.

It implies that the automatic landmark detection algorithm is very susceptible to image quality change. Therefore, it is a sensitive image quality indicator for synthetic cephalograms. For our Type II synthetic cephalograms, due to some inaccurate structures, the SDRs are still not high enough. For example, the mandible angles in Figs. 14(g)-(i) are more blurry than those in Figs. 14(d)-(f) respectively, causing difficulty for the automatic landmark detection algorithm in landmark identification. Nevertheless, as shown in Tab. III, the SDRs in our Type II synthetic cephalograms, which only require two CBCT projections for each synthesis, are still comparable to those in the Type I synthetic cephalograms with the original sigmoid transform and higher than those in the RayCast synthetic cephalograms.

VI. CONCLUSION AND OUTLOOK

In this work, we have proposed a method to synthesize cephalograms from 3D CBCT volumes with improved image contrast based on the optical properties of conventional X-ray films and improved image resolution using SR techniques. We have also proposed a deep learning method to synthesize cephalograms directly from dual 2D X-ray projections for low dose purpose, which achieves higher accuracy compared with using single projection only. The accuracy of the synthesized landmarks is validated preliminary by manual landmark detection and our proposed automatic cephalomatric landmark detection method.

In this work, proof-of-concept experiments have been carried out. In the future, clinical dental CBCT volumes/projections and their corresponding conventional 2D cephalograms are desired for further clinical verifications. One step further, with matching pairs of clinical data, an end-to-end pipeline can be set up, which allows to optimize image contrast and image resolution for optimal automatic landmark detection.

REFERENCES

[1] B. H. Broadbent, "A new X-ray technique and its application to orthodontia," *The Angle Orthodontist*, vol. 1, no. 2, pp. 45–66, 1931.

[2] P. Mozzo, C. Procacci, A. Tacconi, P. T. Martini, and I. B. Andreis, "A new volumetric CT machine for dental imaging based on the cone-beam technique: preliminary results," *European radiology*, vol. 8, no. 9, pp. 1558–1564, 1998.

[3] W. C. Scarfe, A. G. Farman, P. Sukovic *et al.*, "Clinical applications of cone-beam computed tomography in dental practice," *Journal-Canadian Dental Association*, vol. 72, no. 1, p. 75, 2006.

[4] S.-H. Park, H.-S. Yu, K.-D. Kim, K.-J. Lee, and H.-S. Baik, "A proposal for a new analysis of craniofacial morphology by 3-dimensional computed tomography," *Am. J. Orthod. Dentofacial Orthop.*, vol. 129, no. 5, pp. 600–e23, 2006.

[5] H. Kamiishi, Y. Miyasato, and M. Kosaka, "Development of the 3D-cephalogram: a technical note," *Journal of Cranio-Maxillofacial Surgery*, vol. 35, no. 4-5, pp. 258–260, 2007.

[6] P. Pittayapat, N. Limchaichana-Bolstad, G. Willems, and R. Jacobs, "Three-dimensional cephalometric analysis in orthodontics: a systematic review," *Orthodontics & craniofacial research*, vol. 17, no. 2, pp. 69–91, 2014.

[7] C. d. O. Lisboa, D. Masterson, A. F. J. MOTTA, and A. T. Motta, "Reliability and reproducibility of three-dimensional cephalometric landmarks using CBCT: a systematic review," *Journal of Applied Oral Science*, vol. 23, no. 2, pp. 112–119, 2015.

[8] W. C. Scarfe and C. Angelopoulos, *Maxillofacial cone beam computed tomography: principles, techniques and clinical applications*. Springer, 2018.

[9] A. G. Farman, W. C. Scarfe, M. J. Hilgers, O. Bida, M. Moshiri, and P. Sukovic, "Dentomaxillofacial cone-beam CT for orthodontic assessment," in *International Congress Series*, vol. 1281. Elsevier, 2005, pp. 1187–1190.

[10] A. G. Farman and W. C. Scarfe, "Development of imaging selection criteria and procedures should precede cephalometric assessment with cone-beam computed tomography," *Am. J. Orthod. Dentofacial Orthop.*, vol. 130, no. 2, pp. 257–265, 2006.

[11] M. Moshiri, W. C. Scarfe, M. L. Hilgers, J. P. Scheetz, A. M. Silveira, and A. G. Farman, "Accuracy of linear measurements from imaging plate and lateral cephalometric images derived from cone-beam computed tomography," *Am. J. Orthod. Dentofacial Orthop.*, vol. 132, no. 4, pp. 550–560, 2007.

[12] V. Kumar, J. Ludlow, A. Mol, and L. Cevidanes, "Comparison of conventional and cone beam CT synthesized cephalograms," *Dentomaxillofacial Radiol.*, vol. 36, no. 5, pp. 263–269, 2007.

[13] P. M. Cattaneo, C. B. Bloch, D. Calmar, M. Hjortshøj, and B. Melsen, "Comparison between conventional and cone-beam computed tomography–generated cephalograms," *Am. J. Orthod. Dentofacial Orthop.*, vol. 134, no. 6, pp. 798–802, 2008.

[14] O. J. van Vlijmen, S. J. Bergé, G. R. Swennen, E. M. Bronkhorst, C. Katsaros, and A. M. Kuijpers-Jagtman, "Comparison of cephalometric radiographs obtained from cone-beam computed tomography scans and conventional radiographs," *Int. J. Oral Maxillofac. Surg.*, vol. 67, no. 1, pp. 92–97, 2009.

[15] H.-S. Hwang, K.-M. Lee, G.-S. Uhm, J.-H. Cho, and J. A. McNamara, "Use of reference ear plug to improve accuracy of lateral cephalograms generated from cone-beam computed tomography scans," *Korean J. Orthod.*, vol. 43, no. 2, pp. 54–61, 2013.

[16] M.-H. Chen, J. Z.-C. Chang, S.-H. Kok, Y.-J. Chen, Y.-D. Huang, K.-Y. Cheng, and C.-P. Lin, "Intraobserver reliability of landmark identification in cone-beam computed tomography-synthesized two-dimensional cephalograms versus conventional cephalometric radiography: a preliminary study," *J. Dent. Sci.*, vol. 9, no. 1, pp. 56–62, 2014.

[17] E. R. Ritenour, "Physics overview of screen-film radiography." *Radiographics*, vol. 16, no. 4, pp. 903–916, 1996.

[18] J. Hatvani, A. Basarab, J.-Y. Tourneret, M. Gyöngy, and D. Kouamé, "A tensor factorization method for 3-D super resolution with application to dental CT," *IEEE Trans. Med. Imaging*, vol. 38, no. 6, pp. 1524–1531, 2018.

[19] J. Hatvani, A. Horváth, J. Michetti, A. Basarab, D. Kouamé, and M. Gyöngy, "Deep learning-based super-resolution applied to dental computed tomography," *IEEE Trans. Radiat. Plasma Med. Sci.*, vol. 3, no. 2, pp. 120–128, 2019.

[20] X. Yi, E. Walia, and P. Babyn, "Generative adversarial network in medical imaging: A review," *Med. Image Anal.*, vol. 58, p. 101552, 2019.

[21] L. Qu, Y. Zhang, S. Wang, P.-T. Yap, and D. Shen, "Synthesized 7T MRI from 3T MRI via deep learning in spatial and wavelet domains," *Med. Image Anal.*, vol. 62, p. 101663, 2020.

[22] K. Armanious, C. Jiang, M. Fischer, T. Küstner, T. Hepp, K. Nikolaou, S. Gatidis, and B. Yang, "Medgan: Medical image translation using GANs," *Comput. Med. Imaging Graph.*, vol. 79, p. 101684, 2020.

[23] B. Stimpel, C. Syben, T. Würfl, K. Breininger, P. Hoelter, A. Dörfler, and A. Maier, "projection-to-projection translation for hybrid X-ray and magnetic resonance imaging," *Sci. Rep.*, vol. 9, no. 1, pp. 1–10, 2019.

[24] C. Syben, B. Stimpel, P. Roser, A. Dörfler, and A. Maier, "Known operator learning enables constrained projection geometry conversion: Parallel to cone-beam for hybrid MR/X-ray imaging," *IEEE Trans. Med. Imaging*, pp. 1–12, 2020.

[25] A. K. Maier, C. Syben, B. Stimpel, T. Würfl, M. Hoffmann, F. Schebesch, W. Fu, L. Mill, L. Kling, and S. Christiansen, "Learning with known operators reduces maximum error bounds," *Nat. Mach. Intell.*, vol. 1, no. 8, pp. 373–380, 2019.

[26] W. Yang, X. Zhang, Y. Tian, W. Wang, J.-H. Xue, and Q. Liao, "Deep learning for single image super-resolution: A brief review," *IEEE Transactions on Multimedia*, vol. 21, no. 12, pp. 3106–3121, 2019.

[27] C. Dong, C. C. Loy, K. He, and X. Tang, "Image super-resolution using deep convolutional networks," *IEEE Transactions on Pattern Analysis and Machine Intelligence*, vol. 38, no. 2, pp. 295–307, 2015.

[28] J. Kim, J. Kwon Lee, and K. Mu Lee, "Accurate image super-resolution using very deep convolutional networks," in *Proc. CVPR*, 2016, pp. 1646–1654.

[29] W.-S. Lai, J.-B. Huang, N. Ahuja, and M.-H. Yang, "Deep laplacian pyramid networks for fast and accurate super-resolution," in *Proc. CVPR*, 2017, pp. 624–632.

[30] B. Lim, S. Son, H. Kim, S. Nah, and K. Mu Lee, "Enhanced deep residual networks for single image super-resolution," in *Proc. CVPR*, 2017, pp. 136–144.

[31] J. Kim, J. Kwon Lee, and K. Mu Lee, "Deeply-recursive convolutional network for image super-resolution," in *Proc. CVPR*, 2016, pp. 1637–1645.

[32] C. Ledig, L. Theis, F. Huszár, J. Caballero, A. Cunningham, A. Acosta, A. Aitken, A. Tejani, J. Totz, Z. Wang *et al.*, "Photo-realistic single image super-resolution using a generative adversarial network," in *Proc. CVPR*, 2017, pp. 4681–4690.

[33] Y. Zhang, Y. Tian, Y. Kong, B. Zhong, and Y. Fu, "Residual dense network for image super-resolution," in *Proc. CVPR*, 2018, pp. 2472–2481.

[34] X. Wang, K. Yu, S. Wu, J. Gu, Y. Liu, C. Dong, Y. Qiao, and C. Change Loy, "ESRGAN: Enhanced super-resolution generative adversarial networks," in *Proc. ECCV*, 2018, pp. 0–0.

[35] C.-W. Wang, C.-T. Huang, M.-C. Hsieh, C.-H. Li, S.-W. Chang, W.-C. Li, R. Vandaele, R. Marée, S. Jodogne, P. Geurts *et al.*, "Evaluation and comparison of anatomical landmark detection methods for cephalometric X-ray images: a grand challenge," *IEEE Trans. Med. Imaging*, vol. 34, no. 9, pp. 1890–1900, 2015.

[36] C.-W. Wang, C.-T. Huang, J.-H. Lee, C.-H. Li, S.-W. Chang, M.-J. Siao, T.-M. Lai, B. Ibragimov, T. Vrtovec, O. Ronneberger *et al.*, "A benchmark for comparison of dental radiography analysis algorithms," *Med. Image Anal.*, vol. 31, pp. 63–76, 2016.

[37] B. Ibragimov, B. Likar, F. Pernus, and T. Vrtovec, "Automatic cephalometric X-ray landmark detection by applying game theory and random forests," in *Proc. ISBI*, 2014.

[38] C. Lindner and T. F. Cootes, "Fully automatic cephalometric evaluation using random forest regression-voting," in *Proc. ISBI*. Citeseer, 2015.

[39] S. Ö. Arik, B. Ibragimov, and L. Xing, "Fully automated quantitative cephalometry using convolutional neural networks," *Journal of Medical Imaging*, vol. 4, no. 1, p. 014501, 2017.

[40] J. Qian, M. Cheng, Y. Tao, J. Lin, and H. Lin, "Cephanet: An improved faster R-CNN for cephalometric landmark detection," in *Proc. ISBI*. IEEE, 2019, pp. 868–871.

[41] R. Chen, Y. Ma, N. Chen, D. Lee, and W. Wang, "Cephalometric landmark detection by attentive feature pyramid fusion and regression-voting," in *Proc. MICCAI*. Springer, 2019, pp. 873–881.

[42] Y. Song, X. Qiao, Y. Iwamoto, and Y.-w. Chen, "Automatic cephalometric landmark detection on X-ray images using a deep-learning method," *Appl. Sci.*, vol. 10, no. 7, p. 2547, 2020.

[43] K. He, X. Zhang, S. Ren, and J. Sun, "Deep residual learning for image recognition," in *Proc. CVPR*, 2016, pp. 770–778.

[44] S. Chilamkurthy, R. Ghosh, S. Tanamala, M. Biviji, N. G. Campeau, V. K. Venugopal, V. Mahajan, P. Rao, and P. Warier, "Development and validation of deep learning algorithms for detection of critical findings in head CT scans," *arXiv preprint:1803.05854*, 2018.

[45] P. Isola, J.-Y. Zhu, T. Zhou, and A. A. Efros, "Image-to-image translation with conditional adversarial networks," in *Proc. CVPR*, 2017, pp. 1125–1134.

[46] A. Odena, V. Dumoulin, and C. Olah, "Deconvolution and checkerboard artifacts," *Distill*, vol. 1, no. 10, p. e3, 2016.

[47] Y. LeCun, L. Bottou, Y. Bengio, and P. Haffner, "Gradient-based learning applied to document recognition," *Proc. IEEE*, vol. 86, no. 11, pp. 2278–2324, 1998.

[48] H. Lee, M. Park, and J. Kim, "Cephalometric landmark detection in dental X-ray images using convolutional neural networks," in *Medical Imaging 2017: Computer-Aided Diagnosis*, vol. 10134, 2017, p. 101341W.